Turbulent Flow over Low-Order Models of Highly Irregular Surface Roughness

B. E. Johnson[*] and K. T. Christensen[†]

University of Illinois at Urbana–Champaign, Urbana, Illinois 61801

Low-order representations of surface roughness replicated from a turbine blade damaged by spallation (denoted as "full surface") are devised using singular value decomposition, and the impact of these low-order surface models is assessed in turbulent channel flow. The intent of this effort is to determine the level of topographical detail of the full surface that is required to reproduce the statistical character of turbulent flow over the full surface. Particle-image velocimetry measurements of flow at a fixed Reynolds number over a smooth surface, the full surface, and four low-order representations of the full surface reveal that a surface model based on the first 20 basis functions of the decomposition (9% of the total number of modes) yields an accurate reproduction of the statistics of flow over the full surface. In particular, the mean velocity profile, profiles of the Reynolds normal and shear stresses, and even the instantaneous turbulent events that contribute heavily to the generation of turbulent shear stress as assessed via quadrant analysis show consistency for flow over this low-order model as well as the full surface. Because the low-order modes included in these models reflect only the large-scale topographical features of the full surface (meaning finer-scale topographical details are excluded), these observations indicate that the larger-scale features of the full surface predominantly dictate its impact on the flow.

Nomenclature

a	=	coefficient of expansion
H	=	hyperbolic hole size
h	=	channel half-height, m
I	=	indicator function
k	=	average peak-to-valley roughness height, m
L	=	total number of singular value decomposition basis functions
M	=	number of basis functions included in the low-order model
N	=	space fraction
P	=	total number of streamwise grid points in an ensemble
Re_τ	=	friction Reynolds number
S	=	stress fraction
u	=	total streamwise velocity, m/s
u'	=	fluctuating streamwise velocity, m/s
$u'v'$	=	instantaneous Reynolds shear stress, m^2/s^2
u_τ	=	friction velocity, m/s
v	=	total wall-normal velocity, m/s
v'	=	fluctuating wall-normal velocity, m/s
x	=	streamwise direction, m
y	=	wall-normal direction, m
y_*	=	viscous length scale, m
z	=	spanwise direction, m
α	=	singular value, m
Δ	=	particle-image velocimetry grid spacing, m
η	=	fluctuating surface elevation, m
ν	=	kinematic viscosity of fluid, m^2/s
ρ	=	density of fluid, kg/m^3
τ_w	=	wall shear stress, Pa
ϕ	=	basis function
$\langle \cdot \rangle$	=	ensemble and streamwise average

Subscripts

cl	=	centerline of channel
full	=	full surface
i	=	variable number
j	=	mode number
low	=	low-order model
max	=	maximum value
Q	=	quadrant (1–4) in $u'-v'$ plane
res	=	residual

Superscripts

+	=	normalization in inner units
SM	=	smooth-wall value

I. Introduction

THE interaction of a turbulent flow with an abrupt transition from smooth- to rough-wall conditions initiates the development of an internal layer whose thickness grows as it traverses downstream [1]. In this context, the flow remains unaffected by the roughness outside the boundary of the internal layer, whereas the flow within this layer can be altered significantly. Understanding the flow physics associated with abrupt transitions in surface characteristics is important, as such transitions commonly occur in practical engineering systems wherein surface quality can vary considerably along the predominant flow direction [2,3]. However, although the surface quality in practical engineering systems can be highly irregular due to multiple damage mechanisms and vary from aerodynamically smooth before deployment to significantly roughened over time due to cumulative degradation, most studies of rough-wall turbulence have employed idealized roughness, including sand grain, woven mesh, and patterned arrays of elements. Although such topographies are relatively easy to realize in the laboratory setting, their ordered character and narrow spectrum of topographical scales are counter to the surface characteristics of practical flow systems. For example, turbine blades suffer significant surface degradation over their deployment lifetime due to a multitude of mechanisms, most notably deposition of foreign materials, pitting, and spallation [4]. Close inspection of aged turbine blades reveals surface

degradation marked by a broad range of topographical scales as well as a relatively high intermittency of occurrence [4,5]. Other examples of irregular roughness include accumulation of algae and barnacles on the exterior surfaces of submarines and ships [6] as well as cumulative erosion on the blades of windmills operating near the sea. In all of these cases, single-scale roughness arranged in an ordered manner typically employed in laboratory investigations will likely not be representative of the rich topographies encountered in practice. For example, Bons [5] found that classical scalings for skin friction over rough walls, derived for flows over idealized roughness, do not hold for some flows over scaled turbine-blade roughness. Likewise, using flow over a short distance of damaged turbine-blade roughness, Wu and Christensen [7] found that large-scale local topographical features of a random surface may significantly enhance local Reynolds shear stress within the internal layer of this developing flow. For developed flow, wherein the internal layer has grown to engulf the entire boundary-layer thickness, Wu and Christensen [8] reported that the turbulence statistics outside the roughness sublayer remained relatively unaffected by the roughness replicated from a turbine blade damaged by deposition materials (compared with smooth-wall flow) when one accounts for the increased drag at the surface when scaling the statistics. However, such similarity likely will not exist in the case of developing flows for which the internal layer has not grown to occupy the entire wall-normal extent of the boundary layer. Thus, it is possible that the effect of idealized roughness conditions upon wall-bounded turbulence, particularly in the case of abrupt transition from smooth-to rough-wall conditions, may be insufficient for the successful modeling or control of practical flows in the presence of irregular roughness, particularly in the case of developing flows.

Of interest in the area of practical roughness is the relative impact that each topographical scale of a surface has on the flow. That is, are flows over irregular roughness predominantly governed by the impact of the largest roughness scales or do the finer surface features contribute in an important manner? Schultz and Flack [9] considered this effect in the context of idealized roughness by studying the flow over uniform spheres and the same topography with the addition of finer-scale grit roughness. They reported good agreement between the Reynolds stress profiles for flow over both surfaces throughout the boundary layer, indicating little effect of finer-scale roughness on the turbulence. However, it is not clear how this study of two roughness scales of substantially different size translates to the case of practical roughness, which is marked by a broad spectrum of topographical scales. With respect to more practical roughness, Itoh et al. [10] measured turbulent flow over the fur surface of a seal that exhibited a ribletlike character, though both the amplitude and wavelength of these topographical features varied significantly in space. Itoh et al. [10] also made measurements of turbulent flow over a model of the seal fur that consisted of ordered riblets manufactured with the dominant amplitude and wavelength of the seal fur. A comparison of these results highlighted the lack of consistency in the turbulence statistics for flow over the real seal surface and the model. These differences highlight the importance of topographical characteristics beyond simply the dominant amplitude and wavelength of the real surface in determining the overall impact of the rough surface on the flow.

The present effort considers the development of low-order topographical models of highly irregular surface roughness replicated from a turbine blade damaged by spallation. Singular value decomposition is used to decompose the complex surface topography into a set of spatial basis functions of decreasing importance. Only the most dominant of these basis functions are used to reconstruct the surface topography, meaning that a substantial fraction of the larger-scale-surface features are included in the low-order models whereas the finer topographical details are excluded. Short streamwise fetches of these low-order representations are then built using rapid-prototyping methods and tested in turbulent channel flow to assess how well they reproduce the flow modifications generated by the full-surface topography. Such comparisons are meant to reveal the relative importance of finer-compared with larger-scale roughness features in the context of practical roughness.

II. Experiments

A. Flow Facility

Experiments are performed with air as the working fluid in a closed-loop channel-flow facility with a development length of $216h$, where $h = 25.4$ mm is the half-height of the channel. The aspect ratio of the spanwise width to wall-normal height of the channel is $10.125:1$, yielding two-dimensional flow conditions along the spanwise centerline of the channel. Upstream of the channel development length, the flow is guided through a perforated plate, honeycomb, and a series of screens and is then contracted into the channel where it is immediately tripped by 36-grit sandpaper placed along the top and bottom channel surfaces. These flow-conditioning methods have been shown in past studies to generate high-quality turbulent channel-flow conditions [11,12]. The air in the channel is circulated back to the blower, which allows a steady temperature state to be attained within the channel. This steady temperature, along with the atmospheric pressure, is used to determine the density of the air, ρ, using the ideal gas law and its kinematic viscosity, ν, with Sutherland's correlation. Four static pressure taps, mounted near the spanwise centerline in the top wall of the channel at a streamwise spacing of $36h$, allow the measurement of the streamwise pressure gradient from which an independent measure of the wall shear stress, τ_w, is attained. The friction velocity and viscous length scale are then calculated as $u_\tau \equiv \sqrt{(\tau_w/\rho)}$ and $y_* \equiv \nu/u_\tau$, respectively.

B. Rough Surfaces

The rough surface employed in this effort is the same as that recently studied by Wu and Christensen [7] and is a scaled version of a profilometric surface scan of a turbine blade damaged by spallation first reported in Bons et al. [4,5]. Bons et al. [4] used a contact stylist profilometry system with a stylus tip radius of 1.5 μm, which limited the smallest resolvable topographical features to a few microns in size. This surface, shown in Fig. 1, is highly irregular and contains a broad range of topographical scales. In particular, large-scale surface defects are accompanied by much finer-scale topographical features. The general characteristics of this surface are representative of the surface roughness encountered in many practical flows of interest, yet are quite distinct from the "idealized" roughness typically studied in the laboratory, including sand grain, mesh, and ordered arrays of elements. The average peak-to-valley height of this surface is $k_{full} = 1.35$ mm, and the rms roughness height (about the mean elevation) is $k_{full}^{rms} = 0.31$ mm. Because k is usually taken as a representative measure of the roughness height [5], the ratio of the channel half-height to k_{full} is $h/k_{full} = 18.8$ for the present study.
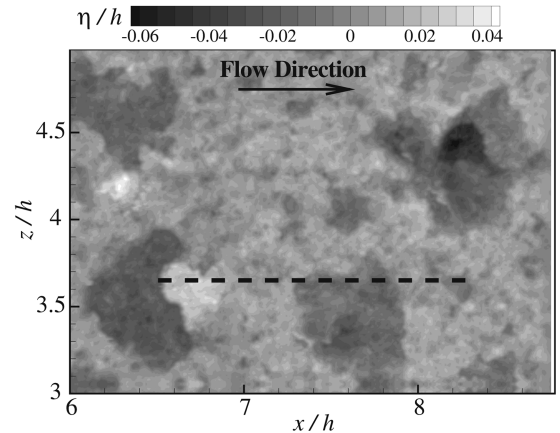

Fig. 1 Topographical map of the turbine-blade roughness considered in the present effort. Dashed line demarcates the PIV measurement location.

This surface is hereafter referred to as the "full surface" upon which the low-order representations are based.

The low-order reconstructions considered herein are devised using the singular value decomposition (SVD) of the fluctuating topography about the mean elevation. This methodology is akin to proper orthogonal decomposition (POD) as it provides an optimal basis for describing an inhomogeneous signal of interest. (Only the details of SVD directly pertinent to the present application are presented herein. The reader is directed to Chatterjee [13], for example, for a more detailed discussion.) With regard to the present effort, the fluctuating surface elevation of the full surface, $\eta_{\text{full}}(x, z)$, shown in Fig. 1 can be decomposed as

$$\eta(x, z) = \sum_{j=1}^{L} a_j \phi_j(x, z) \qquad (1)$$

where a_j are the coefficients of the expansion, ϕ_j represent orthogonal basis functions, and L represents the total number of basis functions. Using this decomposition, one can approximate the fluctuating surface elevation of the full surface as

$$\eta_{\text{full}}(x, z) \approx \eta_{\text{low}}^M(x, z) = \sum_{j=1}^{M} a_j \phi_j(x, z) \qquad (2)$$

where η_{low}^M is referred to as the low-order (or reduced-order) representation of η_{full} based on only the first M ($<L$) modes of the decomposition. Therefore, some detail of the original surface is lost in the low-order reconstruction. Also note that inclusion of all basis functions in this reconstruction recovers the full-surface topography ($\eta_{\text{low}}^L = \eta_{\text{full}}$).

The basis functions and coefficients of the expansion in Eq. (1) are determined using SVD. In this context, one can write the topographical information contained in $\eta_{\text{full}}(x, z)$ in the form of a matrix $\mathbf{A}$, and this matrix can be decomposed by SVD as

$$\mathbf{A} = \mathbf{U}\boldsymbol{\Sigma}\mathbf{V}^T \qquad (3)$$

where $\mathbf{U}$ and $\mathbf{V}$ are orthogonal matrices, and $\boldsymbol{\Sigma}$ is a diagonal matrix containing the singular values of $\mathbf{A}$, α_n, arranged by decreasing value. Relating this back to POD, the squares of the singular values, $\lambda_j = \alpha_j^2$, represents the eigenvalues of $\mathbf{A}\mathbf{A}^T$ or $\mathbf{A}^T\mathbf{A}$, whereas the columns of $\mathbf{U}$ and $\mathbf{V}$ are related to the eigenvectors of $\mathbf{A}\mathbf{A}^T$ or $\mathbf{A}^T\mathbf{A}$, respectively [13]. For the topography considered herein, $\mathbf{U}$, $\boldsymbol{\Sigma}$, and $\mathbf{V}$ are computed using built-in SVD functions within the MATLAB® software package, and a total of $L = 216$ modes are garnered from the decomposition for the full-surface topography presented in Fig. 1.

The low-order representations of the surface elevation are then devised via SVD as

$$\mathbf{A}_M = \mathbf{U}\boldsymbol{\Sigma}_M\mathbf{V}^T \qquad (4)$$

where only the first M singular values in $\boldsymbol{\Sigma}$ are nonzero and are embodied in the diagonal matrix $\boldsymbol{\Sigma}_M$ [13]. Therefore, the matrix $\mathbf{A}_M$ represents the low-order representation based on the first M modes of the basis or, equivalently, embodies η_{low}^M from Eq. (2). Because the singular values are arranged in descending order, the first M modes represent the most dominant modes of the surface elevation which, as is the case in POD, reflect the larger spatial scales of the original topography. Further, one can show that

$$(k_M^{\text{rms}})^2 = (k_{\text{full}}^{\text{rms}})^2 \frac{\sum_{j=1}^{M} \lambda_j}{\sum_{j=1}^{L} \lambda_j} \qquad (5)$$

where k_M^{rms} and $k_{\text{full}}^{\text{rms}}$ are the rms of the low-order representation containing M modes and the full surface, respectively. We refer to the ratio on the right-hand side of Eq. (5) as the fractional surface content (FSC) of the low-order representation containing the first M modes as it provides a measure of the detail from the full surface retained in the M-order reconstruction.

a)

b)
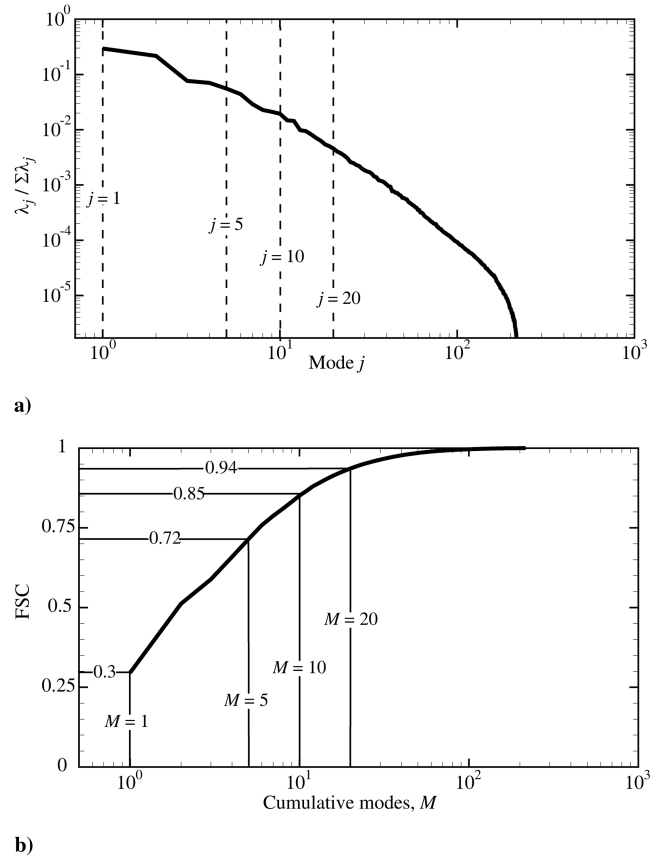
Fig. 2 Spectral characteristics of full-surface topography: a) Eigenvalue spectrum from the SVD as a function of topographical mode, and b) FSC as a function of the number of modes included in the low-order reconstruction (M).

Figure 2a presents the eigenvalue spectrum for the SVD of the full surface presented in Fig. 1, which clearly illustrates the decreasing modal content with increasing mode number. This trend is also noted in Fig. 2b, which presents the FSC versus the number of modes included in the low-order representation (M) of the full surface, and it is evident that the FSC converges quickly toward unity for $M \ll L$. In particular, this plot illustrates the effectiveness of SVD in generating an optimal set of basis functions for which a relatively small subset of these functions retains a significant amount of detail of the full surface. The question under consideration in the present effort is whether low-order reconstructions of the full surface with FSC near unity yet $M \ll L$ generate flow statistics akin to those observed for flow over the full surface.

Replicas of the full surface as well as the low-order models are generated using a rapid-prototyping method based on powder deposition with a spatial resolution of 80 μm. The full surface is fabricated, in addition to four low-order models constructed from the most energetic modes of the aforementioned decomposition: $M = 1$, $M = 5$, $M = 10$, and $M = 20$ (For clarity, $M = 1$ implies only the first basis function is included, $M = 5$ implies the first five basis functions are employed, and so on). The low-order models of the full surface are hereafter referred to by the highest-order mode, M, included in the low-order reconstruction. Figure 3 presents topographical maps of each low-order topographical model, which illustrate the increased topographical detail embodied in the models with increasing modal content. In particular, the $M = 20$ model (Fig. 3d) bears a striking resemblance to the full surface (Fig. 1), which includes all 216 modes. From Fig. 2b, the FSC of the $M = 20$ reconstruction is 0.94, meaning that nearly all of the topographical detail of the full surface is embodied in this model. In contrast, the low-order representation, which includes simply the most energetic mode ($M = 1$; Fig. 3a), only loosely reflects the largest-scale surface defects present in the full surface, which is justified by its relatively
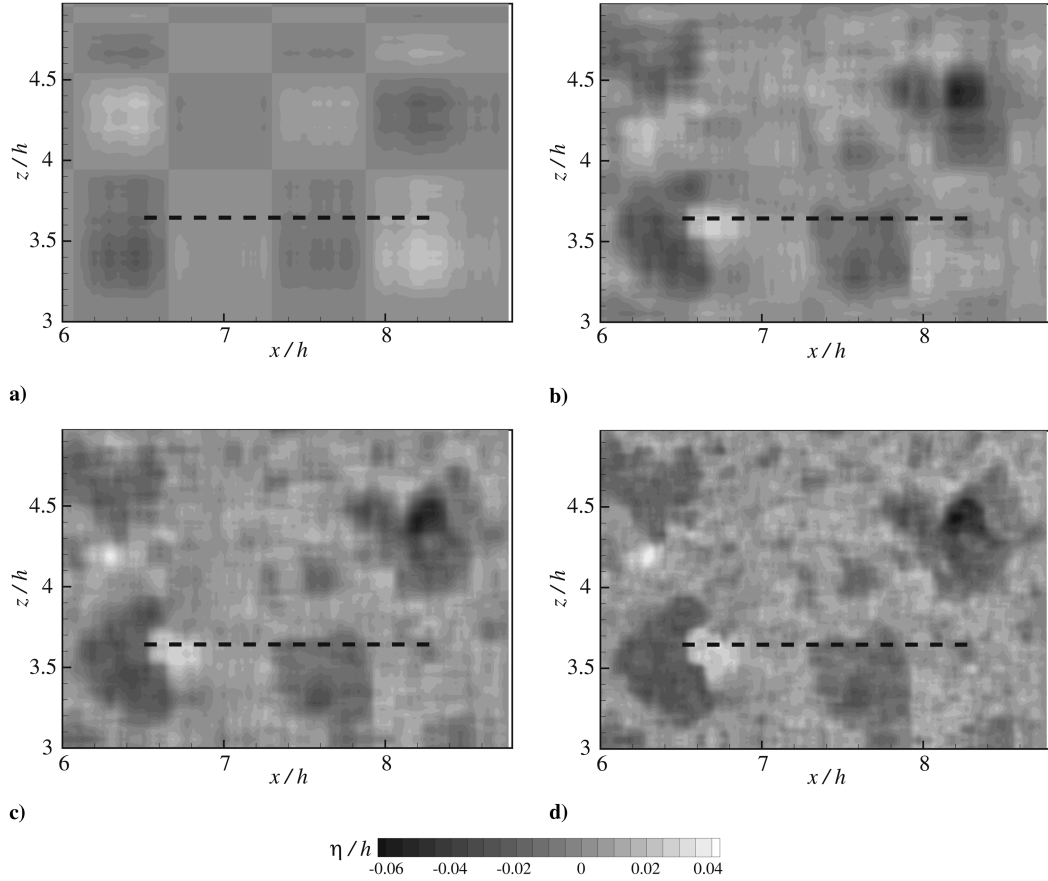
Fig. 3   Topographical maps of the low-order reconstructions of the full surface in Fig. 1: a) $M = 1$, b) $M = 5$, c) $M = 10$, and d) $M = 20$. Dashed lines demarcate the PIV measurement location.

low FSC of 0.3 (Fig. 2b). Finally, the $M = 5$ (Fig. 3b) and the $M = 10$ (Fig. 3c) reconstructions provide excellent examples of how the inclusion of a few additional modes can enhance the quality of the topographical reconstruction of the full surface.

Because the low-order surface representations presented in Fig. 3 are generated by truncating the series representation in Eq. (1) at mode M, there exists a set of residual modes from $M + 1$ to L that represent the surface content excluded in a given low-order representation given by M. One can reconstruct the residual surface features embodied in these excluded modes for a given low-order representation M by computing its associated residual topographical field, η_{res}^{M}, as

$$\eta_{\mathrm{res}}^{M}(x, z) = \eta_{\mathrm{full}}(x, z) - \eta_{\mathrm{low}}^{M}(x, z) = \sum_{j=M+1}^{L} a_j \phi_j(x, z) \qquad (6)$$

Figure 4 presents topographical maps of these residual fields for the $M = 1, 5, 10$, and 20 low-order reconstructions. The contour levels in this figure are consistent with those employed in the maps of the low-order representations themselves (Fig. 3) to facilitate direct comparison. As one would expect, a significant amount of the full-surface content is apparent in the residual field for the $M = 1$ model (Fig. 4a), as its spatial characteristics are nearly indistinguishable from those of the full surface (Fig. 1). This observation is consistent with the fact that the $M = 1$ low-order model contains only 30% of the full-surface content, meaning that the residual field contains 70%. With increasing modal content in the low-order representations, the surface content contained in the residual field reduces considerably until the $M = 20$ case, whose residual topographical field (Fig. 4d) bears little resemblance to the full surface. Instead, the $M = 20$ residual field is marked by weak, smaller-spatial-scale fluctuations in surface topography. The dominance of smaller-spatial-scale topographical fluctuations in this residual field is consistent with the fact that the higher-order modes generated by SVD represent the contributions of smaller-scale spatial features.

Each reconstructed surface is $10h$ long in the streamwise direction and $20.25h$ in the spanwise direction, meaning that the roughness occupies the entire spanwise width of the channel but only extends over a short distance in the flow direction. As such, these experiments represent the abrupt interaction of fully developed, smooth-wall turbulent channel flow with a short streamwise distance of roughness. Smooth leading and trailing edges of $0.38h$ in streamwise length and positioned at the mean elevation of the roughness are manufactured directly into the roughness panels, allowing clean transition from smooth to rough to smooth wall conditions. The roughness panels for a given reconstruction are carefully glued to a cast aluminum plate that is placed along the bottom wall of the channel within a special test section, described in detail in Wu and Christensen [7], that allows accurate adjustment of the vertical position of the roughness relative to the upstream and downstream smooth walls. In this regard, the mean elevation of the roughness is adjusted to be consistent with the upstream and downstream smooth walls to within ± 25 μm using the aforementioned built-in smooth leading and trailing edges as references. Finally, similar to Wu and Christensen [7], each rough-wall condition is periodically extended in the streamwise and spanwise directions because the area of the original surface scan used in the present reconstructions was not sufficient to fill the entire $10 \times 20.25h^2$ area under consideration.

### C.   Particle-Image Velocimetry Details

Measurements of two-dimensional velocity fields (u, v) are made by particle-image velocimetry (PIV) over a $1.8 \times 1.4h^2$ field of view in the streamwise wall-normal $(x–y)$ plane of the flow. Figure 5 presents a schematic of the experimental arrangement. The location of this measurement plane relative to the rough-wall topography under consideration is demarcated by the dashed lines in Figs. 1, 3, and 4. The measurement plane resides over both large-scale topographical features on its upstream end as well as finer-scale
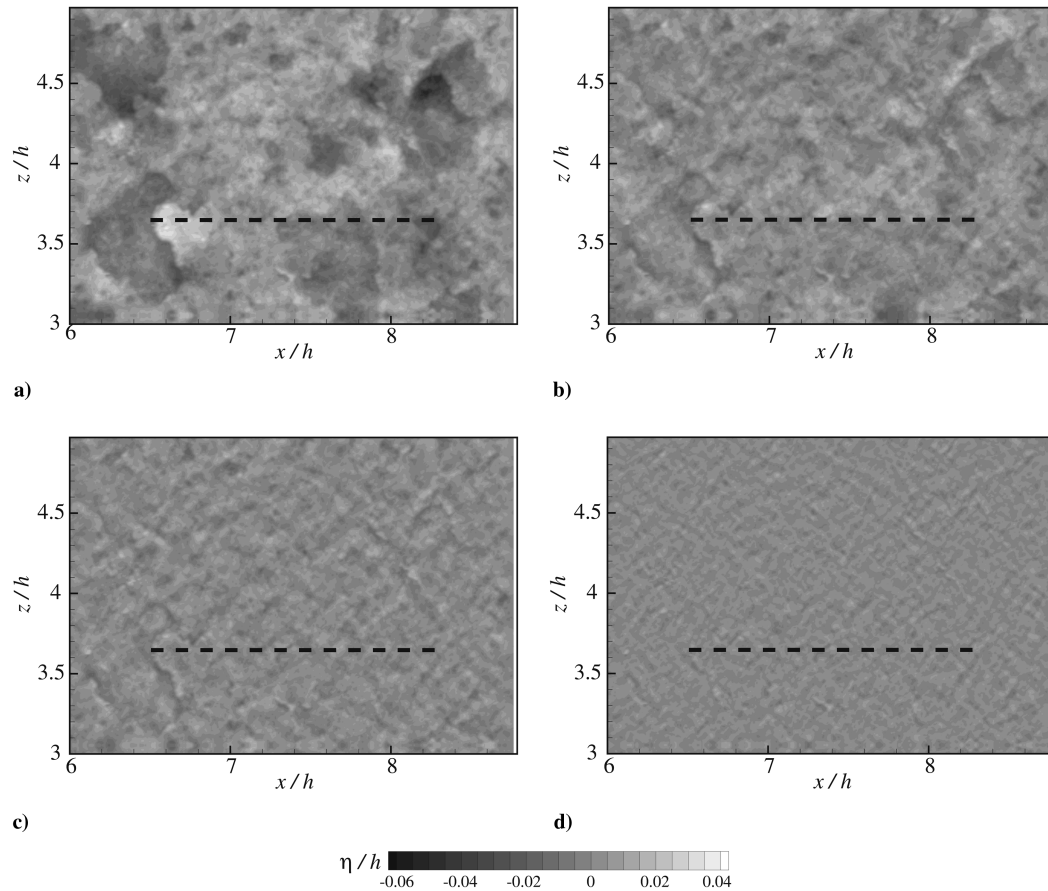
Fig. 4   Topographical maps of the residual fields for the low-order reconstructions presented in Fig. 3: a) $M = 1$, b) $M = 5$, c) $M = 10$, and d) $M = 20$. Dashed lines demarcate the PIV measurement location.

roughness toward its downstream end. It should be noted that the streamwise and spanwise positions of this measurement plane are carefully maintained over the same roughness features for all experiments, allowing a meaningful comparison of the flow statistics. In addition, the measurement plane resides approximately $7h$ downstream of the leading edge of the roughness insert. Measurements of smooth-wall flow are also made in the same test section and at the same streamwise and spanwise positions as the rough-wall tests with an anodized aluminum plate in place of the rough surfaces.

The flow of air is seeded with 1 μm droplets of olive oil generated by a Laskin nozzle that are illuminated by a dual-cavity, pulsed Nd: YAG laser and imaged by a 12-bit frame-straddle charge-coupled device camera operating at 10 Hz with a pixel array of 1300×1000 in the x and y directions, respectively. Pairs of images are interrogated using a two-frame cross-correlation method with first interrogation windows of size 20×20 pixels at 50% overlap to satisfy Nyquist's criterion. Larger second interrogation windows of 22×22 pixels are used, offset by the bulk displacement in the direction of the mean flow (approximately 9 pixels), to reduce errors
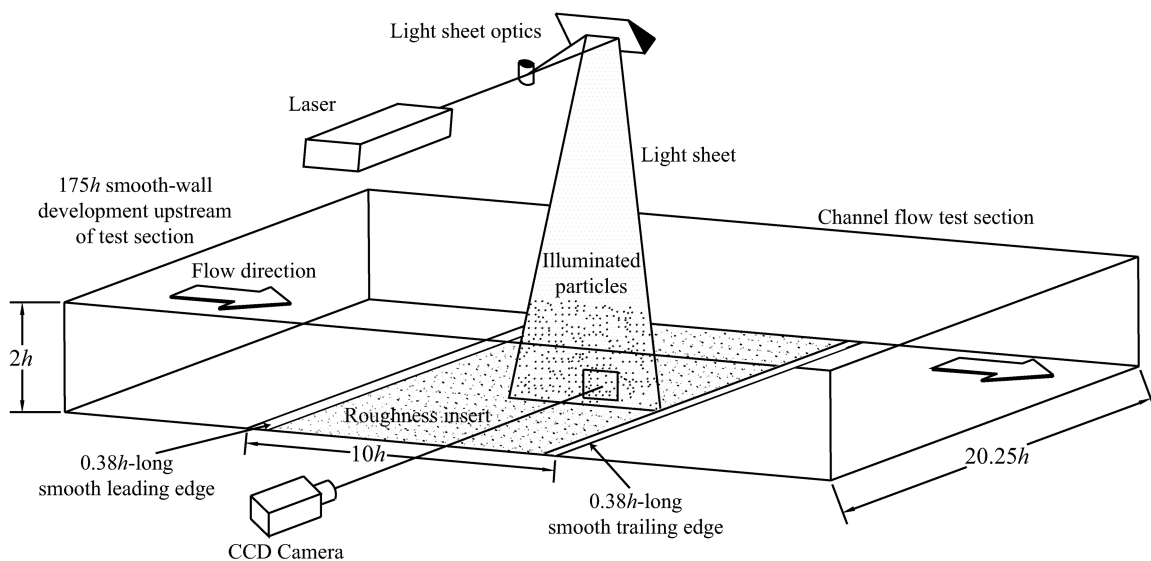
Fig. 5   Schematic of the flow facility and experimental arrangement.

associated with the loss of image pairs. Upon interrogation, the vector fields are validated using standard deviation (4σ criterion), and magnitude difference [$1.5\times$ neighborhood (3×3 grid points) mean criterion] comparisons and erroneous vectors are removed. The necessity for the interpolation of holes is reduced because few vectors are removed ($<2\%$, on average, in each ensemble). Each field is then low-pass filtered through a narrow Gaussian filter to remove noise from frequencies higher than the interrogation sampling rate.

Measurements are made over each surface at approximately the same friction Reynolds number ($Re_\tau = u_\tau^{SM} h / \nu$) of 1825, based on the friction velocity of the smooth-wall flow upstream of the roughness, u_τ^{SM}. The error in determining u_τ^{SM} from the streamwise pressure gradient is estimated to be $\pm 4\%$ based on uncertainties in determining the fluid properties and the uncertainty of the pressure transducer employed for assessing the streamwise pressure gradient. Unfortunately, it was not possible to assess the local friction velocity over the roughness at the measurement location for this developing flow, and so all velocity statistics presented herein are normalized using the upstream smooth-wall values of friction velocity (u_τ^{SM}). However, such a scaling has the advantage of allowing one to directly assess the enhancement of the turbulence by the roughness. Because the roughness under consideration will most likely increase the local skin friction, u_τ^{SM} represents a lower bound and y_*^{SM} represents an upper bound on the actual values of u_τ and y_* over the rough surfaces. As such, the lower bound of the roughness Reynolds number $k_{full}^+ = k_{full} / y_*^{SM}$ is 97 for the full surface based on the average peak-to-valley roughness height. Relevant flow parameters are tabulated in Table 1. Finally, approximately four thousand statistically independent velocity vector fields are acquired for each surface condition to reduce the influence of statistical sampling errors ($<0.5\%$) in the calculation of the single-point turbulence statistics presented herein. In particular, the single-point statistics presented herein are computed by first averaging over each ensemble followed by line averaging over the 120 grid points spanning the streamwise field of view. Whereas the rough-wall flows are necessarily developing due to the formation of internal layers generated by the transition from smooth- to rough-wall conditions, the wall-normal extent of the internal layer grows $<10\%$ over this distance, indicating relatively weak inhomogeneity in x over this domain. Further, the present measurements are made over the same relative surface features in the rough-wall cases, meaning that the single-point statistics presented herein represent the average impact of each roughness representation over the same streamwise domain.

Prasad et al. [14] showed that the random error associated with determining particle displacements in PIV is approximately 5% of the particle-image diameter. In the present study, the mean particle-image diameter is approximately 2 pixels, indicating a random error of 0.1 pixels. Therefore, because the time delay between the PIV images for a given experiment is chosen to yield a bulk displacement of 10–12 pixels, this random error is less than 1% of the full-scale velocity. The influence of this random error on the statistics presented herein is further reduced by computing averages over the four thousand statistically independent velocity realizations acquired per condition. One must also consider two sources of bias error that can appear in PIV measurements. Bias due to loss of image pairs is minimized in the present study because a larger second interrogation window and a bulk window offset are used during interrogation of the PIV images. Bias errors due to the peak-locking effect [15] are also minimized in the present experiment because the particle-image diameters exceed

2 pixels [16]. We therefore estimate the bias errors in our PIV measurements at 1% of the full-scale velocity. (The reader is directed to Westerweel [16], Christensen and Adrian [17], and Christensen [15] for a more comprehensive discussion of PIV measurement errors.) As such, the dominant error in the single-point statistics presented herein is that associated with their normalization by the friction velocity, which, as noted above, is approximately $\pm 4\%$.

III. Results

A. Mean Velocity

The mean velocity profiles for all cases are presented in inner units (U/u_τ^{SM} versus y/y_*^{SM}) in Fig. 6a. For comparison, the expected smooth-wall logarithmic law ($U^+ = (1/\kappa) \ell_n y^+ + A$, where $\kappa = 0.41$ and $A = 5.2$) [18] is also included and, as one would expect, the smooth-wall mean velocity profile agrees well with this logarithmic representation for $100 < y^+ < 0.3h^+$. A deficit in the mean streamwise velocity is clearly evident for the rough-wall cases compared with the smooth-wall baseline. The wall-normal extent of this deficit, which can be interpreted as an internal layer within which roughness directly impacts the flow, is surface dependent, with the full surface showing the largest wall-normal extent of velocity deficit ($y^+ < 550$, $y < 0.3h$). This deficit, consistent with enhanced skin friction over the rough surfaces, increases with increasing modal content and is largest for flow over the full surface. In particular, the profile for the $M = 1$ model collapses on the smooth-wall profile, indicating no effect of this roughness on the mean flow despite this low-order model containing 30% of the full-surface content. In contrast, the mean profile for the $M = 20$ representation collapses well on the profile for the full surface, indicating that the first 20 modes (9% of the 216 total modes) are sufficient for reproducing the impact of the full surface on the mean velocity profile. Finally, the profiles for the $M = 5$ and $M = 10$ representations illustrate a consistent progression toward the profile for the full surface with increasing modal content. These trends are also clearly evident in the outer-scaled mean velocity profiles presented in Fig. 6b.

a)

b)
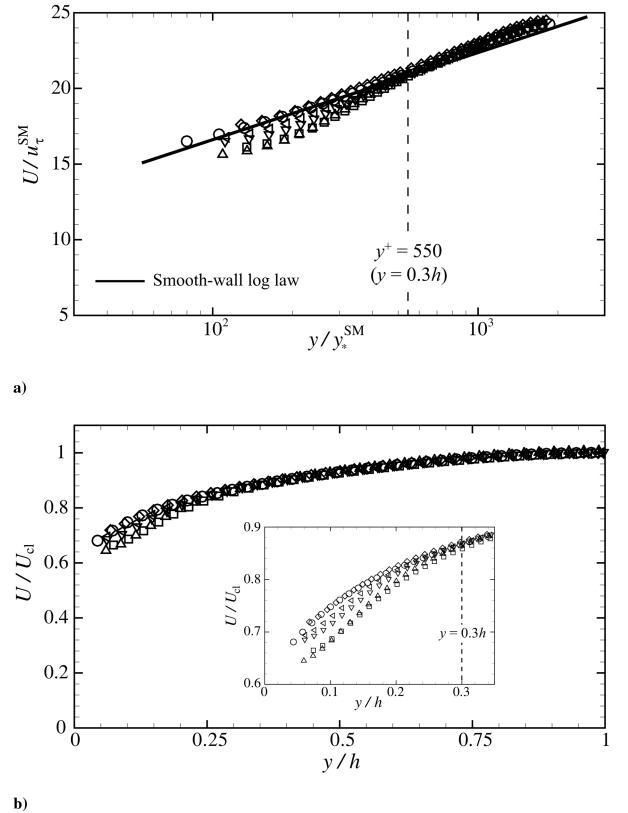
Fig. 6 Mean velocity profiles: a) inner units (normalized with u_τ^{SM} and y_*^{SM}), and b) outer units (normalized with U_{cl} and h). Symbols as in Table 1; not all data points shown for clarity.

Table 1   Summary of flow parameters for all experiments

| Surface	Re_τ	u_τ^{SM}, m/s	y_*^{SM}, μm	FSC	k_M^{rms}, mm	Symbol
Smooth	1828	1.15	13.9	–	–	○
Full	1817	1.15	14.0	1.00	0.310	□
($M = 216$)						
$M = 20$	1830	1.18	13.9	0.94	0.300	△
$M = 10$	1824	1.15	13.9	0.85	0.285	▽
$M = 5$	1825	1.14	13.9	0.72	0.263	◁
$M = 1$	1818	1.15	14.0	0.30	0.170	◇
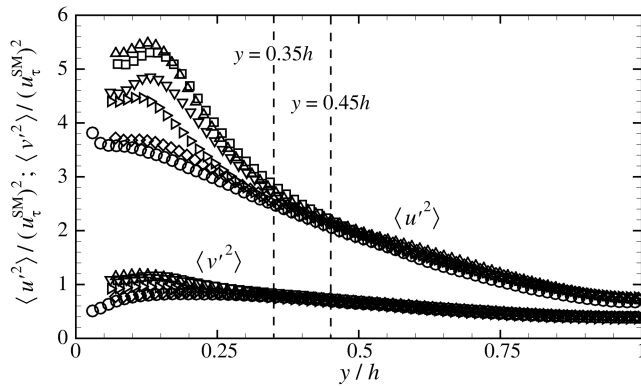
Fig. 7 Profiles of Reynolds normal stresses, $\langle u'^2 \rangle$ and $\langle v'^2 \rangle$, normalized by $(u_\tau^{SM})^2$. Symbols as in Table 1; not all data points shown for clarity.

B. Reynolds Stresses

Figure 7 presents profiles of the streamwise and wall-normal Reynolds normal stresses, $\langle u'^2 \rangle$ and $\langle v'^2 \rangle$, respectively, normalized by $(u_\tau^{SM})^2$. Enhancement of the in-plane Reynolds normal stresses is clearly evident with increasing modal content, with both $\langle u'^2 \rangle$ and $\langle v'^2 \rangle$ enhanced by over 50% in the full-surface case relative to the smooth-wall baseline. With regard to the low-order representations, the $M = 1$ model shows only a slight enhancement of $\langle u'^2 \rangle$ and $\langle v'^2 \rangle$. Consistent with the trends in the mean velocity, the $M = 5$ and 10 models generate progressive enhancement of these turbulent normal stresses with increasing modal content, whereas the $M = 20$ profiles mimic the full-surface results to within the measurement errors of the present experiments. As was noted with the mean velocity, the wall-normal extent of the internal layer formed by the roughness grows with increasing modal content, with the internal layer for flow over the full surface extending to nearly $y = 0.45h$ when measured from $\langle u'^2 \rangle$ and $y = 0.35h$ when assessed from $\langle v'^2 \rangle$. Interestingly, the $\langle v'^2 \rangle$ profiles collapse slightly earlier in y than the $\langle u'^2 \rangle$ profiles. Nevertheless, these wall-normal extents are larger than that noted in the mean velocity profiles, indicating a slightly thicker estimate of the internal layer based on the Reynolds normal stresses.

Similar trends are noted in profiles of the Reynolds shear stress (RSS), $-\langle u'v' \rangle$, normalized by $(u_\tau^{SM})^2$ (Fig. 8). The smooth-wall profile displays the characteristic linear profile in the outer region of the flow along with a distinct peak near $y = 0.1h$. In contrast, the $-\langle u'v' \rangle$ profile for flow over the full surface reveals significant enhancement, with a peak value approximately 50% larger than the smooth-wall baseline. In addition, the wall-normal location of this peak has shifted away from the wall ($y \cong 0.15h$) compared with the smooth-wall result. Farther from the wall, the full-surface profile collapses well with the smooth-wall result for $y > 0.35h$, consistent with the wall-normal location of collapse of the full-surface and smooth-wall $\langle v'^2 \rangle$ profiles. As was observed with the Reynolds normal stresses, the RSS profile for flow over the $M = 20$
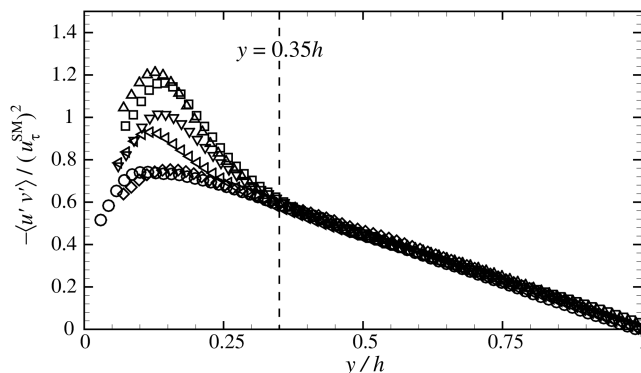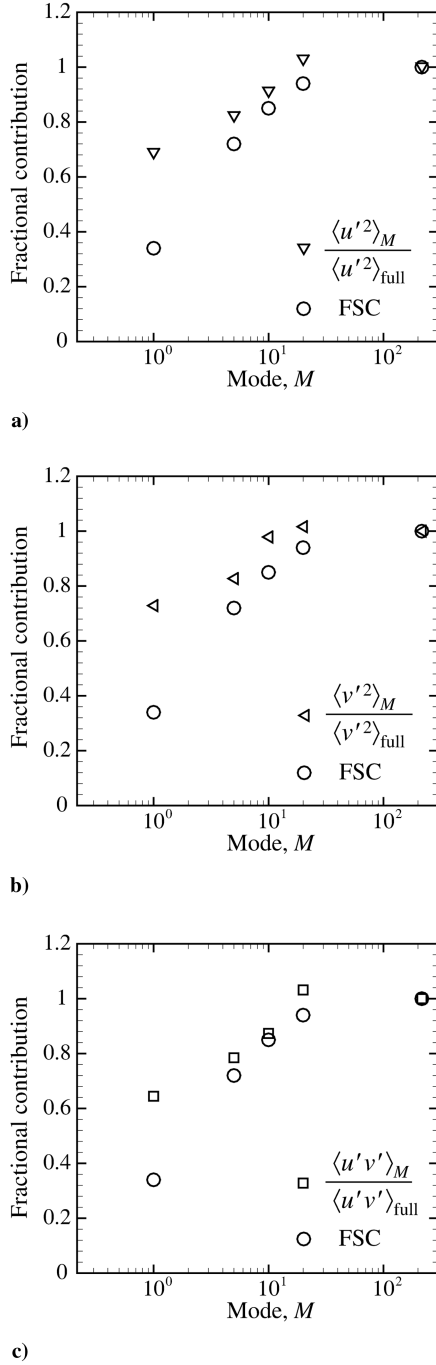
reconstruction is consistent with the full-surface result both in the peak value and wall-normal variation, whereas the $M = 10, 5$, and 1 representations display decreased impact on $-\langle u'v' \rangle$ with decreasing modal content. In particular, the $M = 1$ profile shows little deviation from the smooth-wall profile save for a slight shift in its peak away from the surface. Further, the typical outer-region linear profile in $-\langle u'v' \rangle$ expected in fully developed turbulent channel flow is no longer evident in the rough-wall profiles because these flows can no longer be considered fully developed due to the formation of an internal layer initiated by the abrupt transition from smooth- to rough-wall conditions. Finally, similar to the other statistics presented, the thickness of this internal layer, as measured by collapse of the $-\langle u'v' \rangle$ profiles on the smooth-wall result, also decreases with decreasing modal content.

The Reynolds normal and shear stress profiles presented in Figs. 7 and 8 clearly support the notion that increased modal content in the low-order representations provides a better reproduction of the impact of the full surface on the flow, with the $M = 20$ representation providing a quite reasonable reproduction of the full-surface flow. Based on this trend, one might ask whether there is any correspondence between the FSC of a given surface model and the fraction of the full-surface Reynolds normal and shear stresses generated by that model. To assess this possibility, the ratio of the Reynolds normal/shear stress generated by each surface model to the Reynolds normal/shear stress observed for flow over the full surface is computed at the wall-normal location of the peak value in the full-surface RSS ($y = 0.15h$). These fractional contributions to the full-surface values of $\langle u'^2 \rangle$, $\langle v'^2 \rangle$, and $\langle u'v' \rangle$ are plotted in Fig. 9 along with the FSC of each low-order reconstruction as a function of M. As one would expect from the results in Figs. 7 and 8, the fractional contributions to the Reynolds normal and shear stresses approach unity with increasing M. Interestingly, however, these fractional contributions increase in a manner quite similar to the FSC with increasing modal content save for the $M = 1$ representation, which shows a strong disparity between the fractional contributions to the Reynolds normal and shear stresses ($\sim$60%) compared with the FSC of this model ($\sim$30%). Although no claims can be made that such a correspondence will hold for any irregular surface and its low-order representations given that the interactions of the flow with any surface are nonlinear in nature, these trends are still quite interesting for the specific surface considered herein.
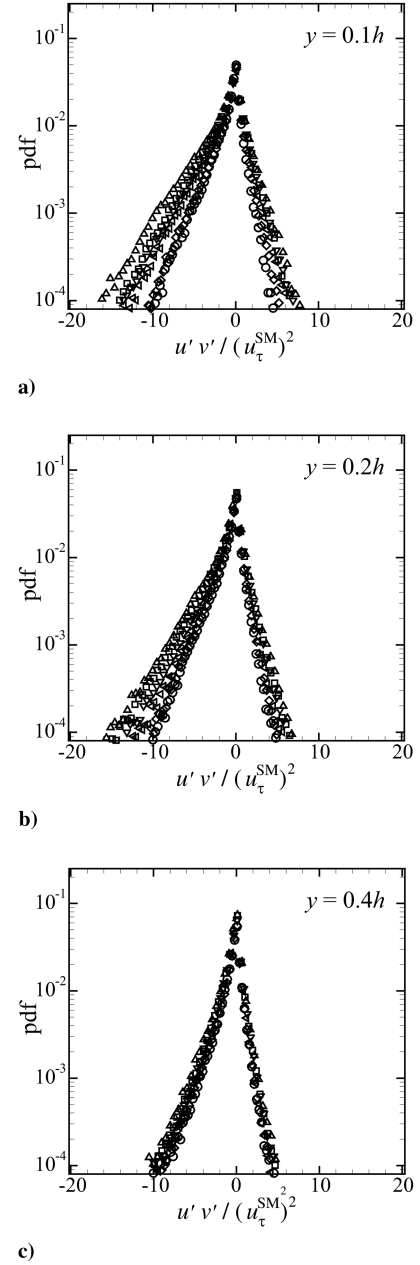
Finally, Fig. 10 presents probability density functions (PDFs) of the $u'v'$ events that contribute to the mean RSS, $\langle u'v' \rangle$, for flow over all surfaces considered herein at various wall-normal locations. In these PDFs, $u'v'$ is normalized by $(u_\tau^{SM})^2$ as a means of directly evaluating modifications of the intensity of the instantaneous $u'v'$ events for flow over the full surface as well as the low-order representations. With regard to smooth-wall flow, the PDFs of $u'v'$ are, in general, skewed toward negative values, particularly close to the wall, which is consistent with the sign (negative) of the mean RSS [19,20]. This behavior is attributable to the dominance of ejection ($u' < 0$, $v' > 0$) and sweep events ($u' > 0$, $v' < 0$) over inward ($u' < 0$, $v' < 0$) and outward ($u' > 0$, $v' > 0$) interactions, both in magnitude as well as frequency of occurrence. The PDF of $u'v'$ for smooth-wall flow becomes symmetric at the centerline, reflecting the flow symmetry of turbulent channel flow. With regard to the impact of the full surface and the low-order surface representations, Fig. 10a presents PDFs at $y = 0.1h$, where $-\langle u'v' \rangle$ displays enhancement compared with the smooth-wall baseline with increased modal content. Consistent with this trend, the PDFs of $u'v'$ show increasingly skewed negative tails with increasing modal content, indicative of the generation of progressively more intense ejection and sweep events. Although the positive tails of the PDFs also show enhancement with increasing modal content, this enhancement is far outweighed by that generated in the negative tails, resulting in a net enhancement of $-\langle u'v' \rangle$ that increases with modal content. The enhancement of both the negative and positive $u'v'$ tails persists with increasing y (Figs. 10b and 10c), though the magnitude of this enhancement decreases until the $u'v'$ PDFs for the various surfaces begin to show consistency for $y \gtrsim 0.35h$, that is, the region of collapse of the various $-\langle u'v' \rangle$ profiles (Fig. 8).

Fig. 8 Profiles of Reynolds shear stress, $-\langle u'v' \rangle$, normalized by $(u_\tau^{SM})^2$. Symbols as in Table 1; not all data points shown for clarity.

a)

a)

b)

b)

c)

c)

Fig. 9   A comparison of the fractional surface content and the fractional contribution to the full-surface values for flow over each low-order representation at $y = 0.15h$ (the peak location in the full surface $-\langle u'v' \rangle$ profile): a) $\langle u'^2 \rangle$, b) $\langle v'^2 \rangle$, and c) $\langle u'v' \rangle$.

Fig. 10   Probability density functions of instantaneous $u'v'$ events contributing to the mean RSS: a) $y = 0.1h$, b) $y = 0.2h$, and c) $y = 0.4h$. Symbols as in Table 1; not all data points shown for clarity.

C.   Quadrant Analysis

The PDFs presented in Fig. 10 suggest that the progressive increase in the magnitude of $-\langle u'v' \rangle$ in Fig. 8 with increasing topographical modal content is associated with an increase in the generation of negative $u'v'$ events. This trend is particularly notable near the surface where the impact of roughness is most pronounced. As noted earlier, however, Reynolds shear stress can be produced by four types of instantaneous $u'v'$ events depending upon which quadrant, Q, in the u'–v' plane a given event resides. This decomposition methodology, termed quadrant analysis by Wallace et al. [19] and Lu and Willmarth [20], leads to the separation of RSS-producing $u'v'$ events into outward interactions (Q_1: $u' > 0$, $v' > 0$), ejections (Q_2: $u' < 0$, $v' > 0$), inward interactions (Q_3: $u' < 0$,

$v' < 0$), and sweeps (Q_4: $u' > 0$, $v' < 0$). Because $\langle u'v' \rangle$ is negative, the contributions of ejections and sweeps must outweigh those of the inward and outward interactions. However, in the present context it is not clear whether the intense negative $u'v'$ events observed in the aforementioned PDFs and the resulting enhancement of the mean RSS are associated with an increased number of ejections, sweeps, or both. Therefore, quadrant analysis is employed to identify the dominant contributors to the generation of RSS with particular interest in understanding the impact of topographical modal content on these trends. In quadrant analysis, the mean RSS at each wall-normal position can be decomposed into contributions from four quadrants ($Q = 1$–4), excluding a hyperbolic hole of size H, as

$$\langle u'v' \rangle_Q(y; H) = \frac{1}{P} \sum_{i=1}^{P} u'(x_i, y) v'(x_i, y) I_Q(x_i, y; H) \qquad (7)$$

where the indicator function, I_Q, is defined as

$$I_Q(x_i, y; H) = \begin{cases} 1 & \text{when } |u'(x_i, y)v'(x_i, y)|_Q \geq H|\langle u'v'\rangle|_{\text{max}}^{\text{SM}} \\ 0 & \text{otherwise} \end{cases}$$

(8)

and P is the total number of grid points at each wall-normal position. In Eq. (8), H represents a nonzero hole size that acts as a threshold to exclude $u'v'$ events of small magnitude to determine the relative contributions of the more intense $u'v'$ events. In this regard, the threshold of I_Q is based on the peak magnitude of the smooth-wall RSS, $|\langle u'v'\rangle|_{\text{max}}^{\text{SM}}$, so that one can clearly identify enhancement of RSS-producing events by the various rough surfaces compared with the smooth-wall baseline. Further, the summation in Eq. (7) represents an ensemble average followed by a line average in the streamwise direction for a fixed wall-normal position. Finally, results are only presented for $y \leq 0.45h$ because this is the domain occupied by the internal layer generated by the rough surfaces.

Quadrant analysis yields three quantities that are of particular interest in assessing the contributions of the four quadrant events to $\langle u'v'\rangle$ for flow over the various surfaces. The first is the RSS contributed by each of the aforementioned events for a given H: $\langle u'v'\rangle_Q(y; H)$ [Eq. (7)]. Alternatively, one can recast this contribution of each quadrant event to the mean RSS for a given H as a stress fraction, S_Q, of the form

$$S_Q(y; H) = \frac{\langle u'v'\rangle_Q(y; H)}{\langle u'v'\rangle(y)}$$

(9)

Finally, the fraction of space, N_Q, occupied by each of the aforementioned events for a given H is defined as

$$N_Q(y; H) = \frac{\sum_{i=1}^{P} I_Q(x_i, y; H)}{P}$$

(10)

These quantities are computed for $Q = 1$–4 for hole sizes of $H = 0$ and 5, that is, inclusion of all and only the most intense RSS-producing events, respectively.

Figure 11 presents $\langle u'v'\rangle_Q$ for the smooth, full, and low-order model surfaces with a threshold of $H = 0$. Because all RSS-producing events are included in the decomposition for $H = 0$, these profiles represent the total contributions of each quadrant event to the mean RSS. As one would expect, ejections (Fig. 11b) and sweeps (Fig. 11d) dominate the mean RSS regardless of surface condition. However, the magnitude of $\langle u'v'\rangle_2$ and $\langle u'v'\rangle_4$ shows clear dependence on the modal content of the low-order surface models. Consistent with the trends in the mean RSS (Fig. 8), the $M = 1$ surface generates ejection and sweep contributions to the mean RSS that are comparable to those found for smooth-wall flow. With increasing modal content, however, both $\langle u'v'\rangle_2$ and $\langle u'v'\rangle_4$ increase in magnitude for fixed y, with the $M = 20$ surface yielding a reasonable approximation of the full-surface results. It is also worth noting that, whereas the contributions of outward and inward interactions ($\langle u'v'\rangle_1$ and $\langle u'v'\rangle_3$, respectively) are 3–4 times smaller than those of ejections and sweeps, their magnitudes are enhanced slightly with increasing modal content, particularly in the vicinity of the wall. However, although these absolute contributions of the four quadrant events for $H = 0$ show clear dependence on modal content, the stress fractions, S_Q, for the various surfaces collapse well except in the immediate vicinity of the wall, where a slight enhancement is noted for the rough-wall cases (Fig. 12). Similarly, the fraction of space occupied by the four quadrant events for $H = 0$ shows little dependence on surface conditions, with all surfaces yielding similar values of N_Q regardless of wall-normal position (Fig. 13).

Figure 14 presents $\langle u'v'\rangle_Q$ for an increased threshold of $H = 5$. Such a threshold eliminates weak $u'v'$ contributions to the mean RSS, allowing one to quantify the role of the most intense $u'v'$ events in determining the mean RSS. Because of this increased threshold, the magnitude of $\langle u'v'\rangle_Q$ decreases considerably compared with the $H = 0$ results. For reference, the $H = 5$ contributions associated with outward and inward interactions ($\langle u'v'\rangle_1$ and $\langle u'v'\rangle_3$, respectively) are essentially zero regardless of wall-normal location and are therefore not presented. In contrast, $\langle u'v'\rangle_2$ and $\langle u'v'\rangle_4$ still both contribute substantially to the mean RSS with their contributions increasing with increased modal content. It should be noted, however, that ejections contribute approximately 1.5 times more than sweeps for the wall-normal range presented, and this trend remains consistent regardless of surface condition. This behavior is clearly reflected in the profiles of the ejection and sweep stress fractions, S_2 and S_4, for $H = 5$ that are presented in Fig. 15. Both of these stress fractions increase significantly with increasing modal content. Interestingly, the $M = 1$ case reveals a slight enhancement
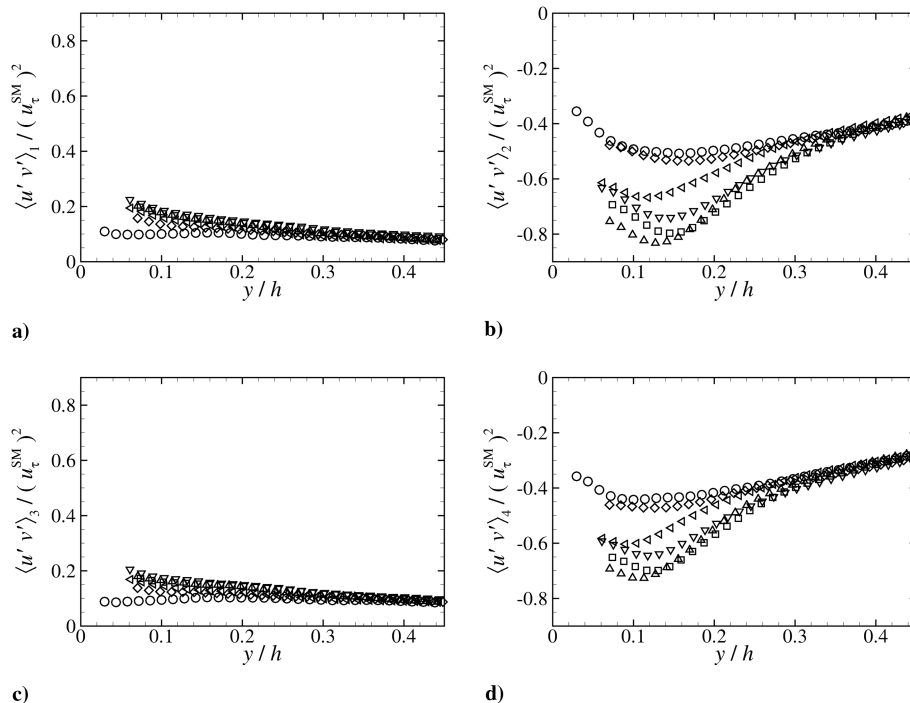

Fig. 11 Quadrant contributions to the mean RSS for $H = 0$: a) $Q = 1$, b) $Q = 2$, c) $Q = 3$, and d) $Q = 4$. Symbols as in Table 1; not all data points shown for clarity.
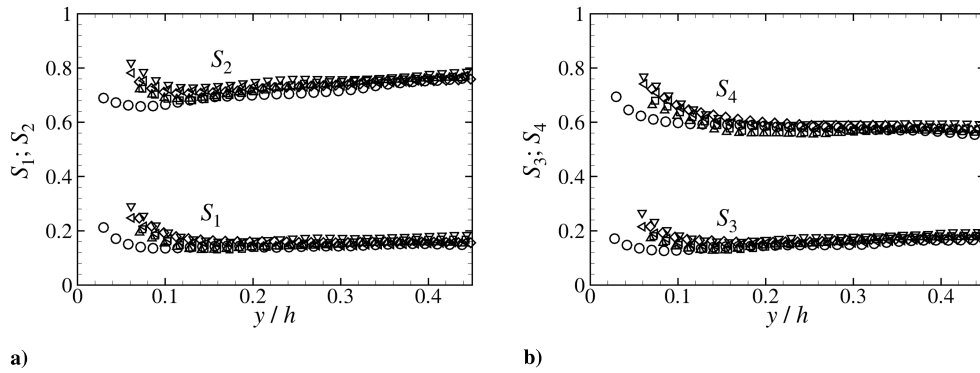
Fig. 12   Stress fractions, S_Q, for $H = 0$. a) $Q = 1$ and 2, and b) $Q = 3$ and 4. Symbols as in Table 1; not all data points shown for clarity.
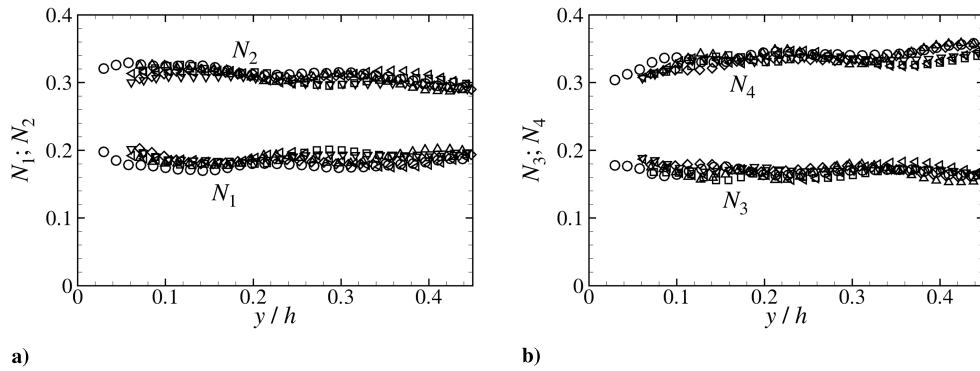

Fig. 13   Space fractions, N_Q, for $H = 0$: a) $Q = 1$ and 2, b) $Q = 3$ and 4. Symbols as in Table 1; not all data points shown for clarity.
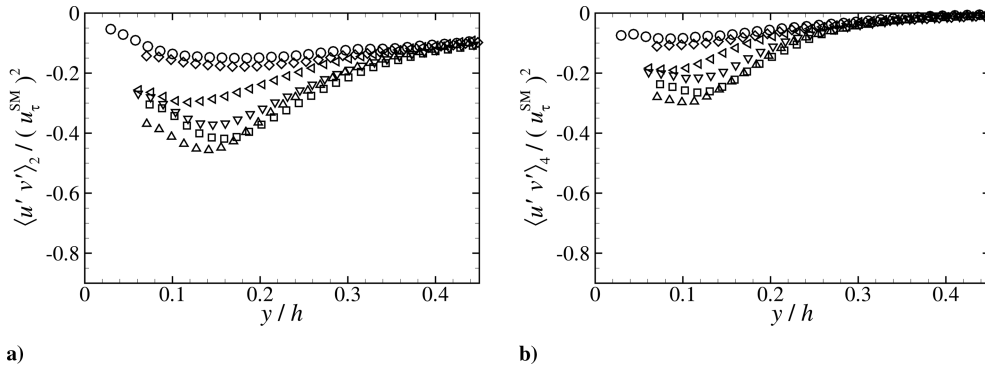

Fig. 14   Contributions to the mean RSS for $H = 5$: a) ejection ($Q = 2$), and b) sweep ($Q = 4$). Symbols as in Table 1; not all data points shown for clarity.
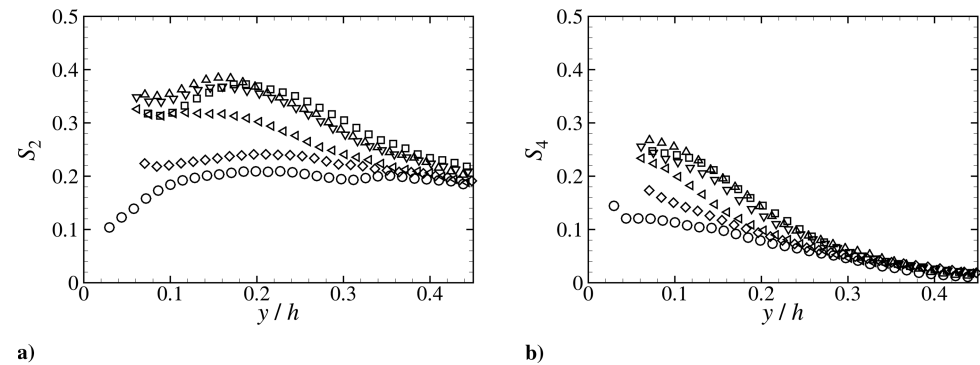

Fig. 15   Stress fractions, S_Q for $H = 5$: a) $Q = 2$, and b) $Q = 4$. Symbols as in Table 1; not all data points shown for clarity.

of the most intense ejection and sweep events even though many of the previous results presented herein indicate strong consistency with the smooth-wall baseline. For the $M = 20$ and full-surface cases, intense ejections satisfying $H = 5$ contribute to approximately 35%

of the mean RSS for $y < 0.2\delta$, whereas intense sweeps are responsible for 15–25% of the mean RSS. Further, Fig. 16 presents the space fractions associated with ejections and sweeps for a threshold of $H = 5$ and, in contrast to the space fractions for $H = 0$, a
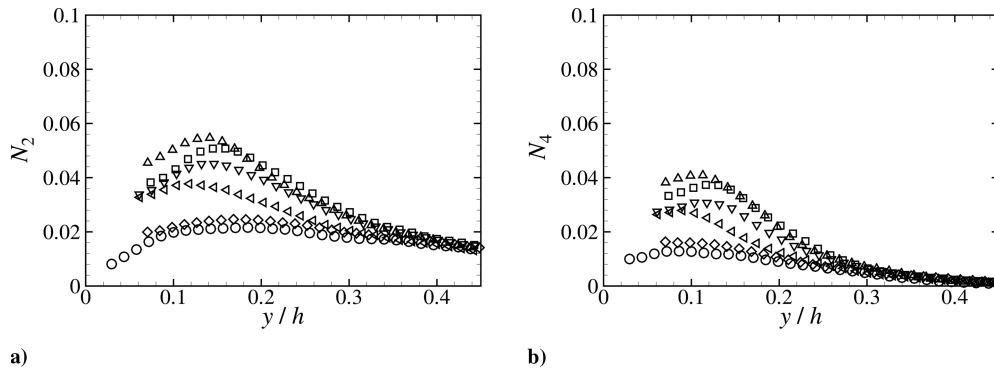
Fig. 16   Space fractions, N_Q, for $H = 5$: a) $Q = 2$, and b) $Q = 4$. Symbols as in Table 1; not all data points shown for clarity.

clear dependence on surface content is noted. In particular, both N_2 and N_4 increase with increasing modal content compared with the smooth-wall baseline. Finally, with respect to reproducing the RSS physics of the full surface, the $M = 20$ representation yields quadrant analysis results that are quite consistent with those of the full surface for both thresholds considered ($H = 0$ and 5). This consistency indicates that the larger-scale-surface features play a defining role in the generation of turbulent stress.

IV.   Conclusions

The development of low-order representations of irregular surface roughness is considered, and the fidelity of these low-order models in recreating the flow modifications noted for turbulent flow over the full surface is quantified. The present effort focuses on surface roughness replicated from a turbine blade damaged by spallation that is marked by a broad range of topographical scales. Particle-image velocimetry measurements of flow at fixed Re over a smooth wall, the full surface, and four low-order representations containing increasing surface detail reveal that a model containing approximately 9% of the total number of modes embodied in the full surface (20 of the 216 total modes) generates flow statistics consistent with flow over the full surface both in terms of their magnitude as well as with respect to the wall-normal extent of the internal layer generated by the roughness. This consistency holds for the mean velocity profile, profiles of the Reynolds normal and shear stresses, and even in the instantaneous turbulent events that contribute heavily to the generation of turbulent shear stress as assessed via quadrant analysis. The present experiments also reveal that decreased modal content generates progressively less surface impact on the flow, with the single-mode representation behaving in a manner consistent with smooth-wall flow despite the fact that this model contains approximately 30% of the full-surface topographical detail.

Finally, given the observed correspondence between the turbulence statistics for flow over the $M = 20$ model to those for flow over the full surface (despite the model containing only 9% of the spatial basis functions of the full surface), it can be concluded that the larger-scale topographical characteristics of the full surface considered herein define its impact on the flow. As such, the smaller-scale topographical details excluded in the $M = 20$ model apparently have little, if no, measurable impact on the character of the turbulence. Although the validity of this observation is likely to be surface dependent, these results do suggest that complex surface roughness can be effectively modeled by only considering the impact of its larger-scale topographical features. Of further interest is the validity of these observations for *developed* flows, wherein the internal roughness layer has grown to occupy the entire wall-normal extent of the flow.

References

[1] Smits, A., and Wood, D., "The Response of Turbulent Boundary Layers to Sudden Perturbations," *Annual Review of Fluid Mechanics*, Vol. 17, 1985, pp. 321–358.
doi:10.1146/annurev.fl.17.010185.001541

[2] Antonia, R., and Luxton, R., "The Response of a Turbulent Boundary Layer to a Step Change in Surface Roughness," *Journal of Fluid Mechanics*, Vol. 48, 1971, pp. 721–761.
doi:10.1017/S0022112071001824

[3] Andreopoulos, J., and Wood, D., "The Response of a Turbulent Boundary Layer to a Short Length of Surface Roughness," *Journal of Fluid Mechanics*, Vol. 118, 1982, pp. 143–164.
doi:10.1017/S0022112082001001

[4] Bons, J., Taylor, R., McClain, S., and Rivir, R., "The Many Faces of Turbine Surface Roughness," *Journal of Turbomachinery*, Vol. 123, 2001, pp. 739–748.
doi:10.1115/1.1400115

[5] Bons, J., "St and C_f Augmentation for Real Turbine Roughness with Elevated Freestream Turbulence," *Journal of Turbomachinery*, Vol. 124, 2002, pp. 632–644.
doi:10.1115/1.1505851

[6] Karlsson, R., "Studies of Skin Fiction in Turbulent Boundary Layers on Smooth and Rough Walls," Ph.D. Thesis, Chalmers Inst. of Technology, Göteborg, Sweden, 1980.

[7] Wu, Y., and Christensen, K., "Reynolds-Stress Enhancement Associated with a Short Fetch of Roughness in Wall Turbulence," *AIAA Journal*, Vol. 44, 2006, pp. 3098–3106.
doi:10.2514/1.22357

[8] Wu, Y., and Christensen, K., "Outer-Layer Similarity in the Presence of a Practical Rough-Wall Topography," *Physics of Fluids*, Vol. 19, 2007, p. 085108.
doi:10.1063/1.2741256

[9] Schultz, M., and Flack, K., "Outer Layer Similarity in Fully Rough Turbulent Boundary Layers," *Experiments in Fluids*, Vol. 38, 2005, pp. 328–340.
doi:10.1007/s00348-004-0903-2

[10] Itoh, M., Tamano, S., Iguchi, R., Yokota, K., Akino, N., Hino, R., and Kubo, S., "Turbulent Drag Reduction by the Seal Fur Surface," *Physics of Fluids*, Vol. 18, 2006, p. 062102.
doi:10.1063/1.2212988

[11] Christensen, K., "Experimental Investigation of Acceleration and Velocity Fields in Turbulent Channel Flow," Ph.D. Thesis, Department of Theoretical and Applied Mechanics, Univ. of Illinois at Urbana–Champaign, Urbana, IL, 2001.

[12] Christensen, K., and Adrian, R., "Statistical Evidence of Hairpin Vortex Packets in Wall Turbulence," *Journal of Fluid Mechanics*, Vol. 431, 2001, pp. 433–443.
doi:10.1017/S0022112001003512

[13] Chatterjee, A., "An Introduction to the Proper Orthogonal Decomposition," *Current Science*, Vol. 78, 2000, pp. 808–816.

[14] Prasad, A. K., Adrian, R. J., Landreth, C. C., and Offutt, P. W., "Effect of Resolution on the Speed and Accuracy of Particle Image Velocimetry Interrogation," *Experiments in Fluids*, Vol. 13, 1992, pp. 105–116.
doi:10.1007/BF00218156

[15] Christensen, K. T., "The Influence of Peak-Locking Errors on Turbulence Statistics Computed from PIV Ensembles," *Experiments in Fluids*, Vol. 36, No. 3, 2004, pp. 484–497.
doi:10.1007/s00348-003-0754-2

[16] Westerweel, J., "Fundamentals of Digital Particle Image Velocimetry," *Measurement Science and Technology*, Vol. 8, 1997, pp. 1379–1392.
doi:10.1088/0957-0233/8/12/002

[17] Christensen, K. T., and Adrian, R. J., "Measurement of Instantaneous Eulerian Acceleration Fields by Particle-Image Accelerometry: Method and Accuracy," *Experiments in Fluids*, Vol. 33, No. 6, 2002, pp. 759–769.
doi:10.1007/s00348-002-0488-6

[18] Pope, S. B., *Turbulent Flows*, Cambridge Univ. Press, Cambridge, England, U.K., 2000.

[19] Wallace, J., Eckelmann, H., and Brodkey, R., "The Wall Region in Turbulent Shear Flow," *Journal of Fluid Mechanics*, Vol. 54, 1972, pp. 39–48.
doi:10.1017/S0022112072000515

[20] Lu, S., and Willmarth, W., "Measurements of the Structure of the Reynolds Stress in a Turbulent Boundary Layer," *Journal of Fluid Mechanics*, Vol. 60, 1973, pp. 481–511.
doi:10.1017/S0022112073000315

N. Chokani
Associate Editor